Published in final edited form as:

Magn Reson Med. 2020 May ; 83(5): 1750–1759. doi:10.1002/mrm.28123.

Imaging the Distribution of Iron Oxide Nanoparticles in Hypothermic Perfused Tissues

Hattie L. Ring[1], **Zhe Gao**[2], **Anirudh Sharma**[2], **Zonghu Han**[2], **Charles Lee**[3,9], **Kelvin G. M. Brockbank**[4,5,6], **Elizabeth D. Greene**[4], **Kristi L. Helke**[6], **Zhen Chen**[4], **Lia H. Campbell**[4], **Bradley Weegman**[7], **Monica Davis**[7], **Michael Taylor**[7], **Sebastian Giwa**[7], **Gregory Fahy**[8], **Brian Wowk**[8], **Roberto Pagotan**[8], **John C. Bischof**[2], **Michael Garwood**[1]

[1]Center for Magnetic Resonance Research, Department of Radiology, University of Minnesota, Minneapolis, USA

[2]Department of Mechanical Engineering, University of Minnesota, Minneapolis, USA

[3]Department of Mechanical Engineering and Engineering Science, University of North Carolina, Charlotte, USA

[4]Tissue Testing Technologies LLC, North Charleston, USA

[5]Department of Bioengineering, Clemson University, Charleston, USA

[6]Department of Comparative Medicine, Medical University of South Carolina, Charleston, USA.

[7]Sylvatica Biotech, Inc, North Charleston, SC USA

[8]21st Century Medicine, Inc, Fontana, CA, USA

[9]Center for Biomedical Engineering and Science and the Mechanical Engineering and Engineering Science Department

Abstract

Purpose: Herein, we evaluate the use of MRI as a tool for assessing iron oxide nanoparticle (IONP) distribution within IONP perfused organs and vascularized composite allografts (VCAs, i.e. hindlimbs) prepared for cryopreservation.

Methods: MRI was performed on room temperature organs and VCAs perfused with IONPs and were assessed at 9.4T. Quantitative T_1 mapping and T_2*-weighted images were acquired using sweep imaging with Fourier transformation (SWIFT) and gradient echo (GRE) sequences, respectively. Verification of IONP localization was performed through histological assessment and μCT.

Results: Quantitative imaging was achieved for organs and VCAs perfused with up to 642 mM_{Fe} (36 mg_{Fe}/mL), which is above previous demonstrations of upper limit detection in agarose [35.7mM_{Fe} (2 mg_{Fe}/mL)]. The stability of IONPs in the perfusate has an impact on the quality of distribution and imaging within organs or VCA. Finally, MRI provided more accurate IONP

Corresponding Author: Michael Garwood, 1-211B, Center for Magnetic Resonance Research, University of Minnesota, 2021 Sixth Street SE, Minneapolis, MN 55455, gar@cmrr.umn.edu.

localization than Prussian blue histological staining in this system, wherein IONPs remain mainly in the vasculature.

Conclusion: Using MRI, we were able to assess the distribution of IONPs throughout organs and VCAs varying in complexity. Additional studies are necessary to better understand this system and validate the calibration between T_1 measurements and IONP concentration.

Keywords

Iron oxide nanoparticle; SWIFT; T_1, T_2, and T_2* quantitation; MRI; Nanowarming; organ preservation; cryopreservation

Introduction

The short timespan in which tissues remain viable after acquisition currently places an enormous logistical burden on transplantation, regenerative medicine, oncofertility, mass casualty medical counter measures, and a variety of other areas spanning biomedicine and research (1,2). Long-term cryopreservation of viable tissues and organs would revolutionize the way they are recovered, allocated, and used in transplantation. To maintain viability, one promising approach is cryopreservation in an amorphous vitrified phase rather than a crystalline phase (1,3). Practical application of vitrification has been mostly limited to small sample sizes, such as cells and thin tissues, due to the inability to rewarm larger (> 3 mL systems) with sufficient speed and uniformity (2–9). Nanowarming is a new technique that aims to address this by providing uniform and fast heating from iron oxide nanoparticles (IONPs) deployed within and around tissues that can be heated in an alternating magnetic field in the kilohertz (kHz) range. Thus far, this new method has been demonstrated with porcine arteries surrounded by IONPs in volumes ranging from 1 – 50 mL (10). Continuing work has focused on the perfusion of IONPs through the vascularized composite allografts (VCAs) and organs in order to achieve the goals of nanowarming.

Within IONP-perfused organs for nanowarming, the homogeneity of IONP distribution is critical, but not trivial to accomplish. The IONP-distribution results from a complex interplay including but not limited to: stability of IONPs (11), cannulation via arterial/venous routes (12), differential pressure between inlet and effluent cannula during perfusion, vascular resistance, perfusate flow rates, and temperature (13,14). Furthermore, once the IONPs have been washed out of the tissue, there is the possibility that IONPs can remain trapped due to cellular uptake or IONP aggregation (15,16).

The quantification of IONPs using MRI has been demonstrated with low and high IONP concentrations (16–18). Low IONP concentrations (< 0.18 mM_{Fe} or 0.01 mg_{Fe}/mL) can be quantified using gradient-echo (GRE) and spin-echo (SE) pulse sequences. Quantification of high IONP concentrations (> 0.18 mM_{Fe} or 0.01 mg_{Fe}/mL) requires the use of echoless pulse sequences which preserve signal from spins with ultrashort T_2 or T_2*. Recent work has measured the overlap of the ranges of IONP concentrations that can be quantified by GRE, SE, and the echoless pulse sequence SWIFT (sweep imaging with Fourier transformation) (19). Additionally, a correlation between *in vivo* R_1 values and the *ex vivo*

heating (specific absorption rate, SAR_{Fe}) produced by IONPs within organs has been established (16).

Previous nanowarming experiments loaded 17.9 mM_{Fe} (1 mg_{Fe}/mL) IONPs within and around an artery. Quantitative R_1 maps of the loaded artery were acquired using SWIFT, and complete unloading of the IONP from the artery was evaluated with T_2*-weighted images acquired with GRE. Herein, the first pilot studies demonstrate the potential for MRI as a qualitative and quantitative assessment method of IONP loading and unloading within four perfused organ types.

Methods

Materials:

The iron oxide nanoparticle (IONP) used were EMG-308 and PBG-300 from Ferrotec (USA). A 5X concentrated Euro-Collins solution was prepared following a published protocol using Milli-Q water (20). The cryoprotective agents (CPAs) in VS55 were 3.1M dimethyl sulfoxide, 3.1M formamide, and 2.21M 1,2-propanediol in 1X Euro-Collins solution (20). The CPAs in M22 were provided by 21st Century Medicine and has been described elsewhere (21). HEPES was from MP Biomedicals (Santa Ana, CA, USA), D-Glucose was purchased from Macron Fine Chemicals (Allentown, PA, USA), DMSO and formamide were purchased from Fischer Chemicals (Hampton, NH, USA). Chemicals used at 21st Century Medicine were from Fischer Chemicals (Hampton, NH, USA), Spectrum (West Compton, CA, USA) and TCI (Portland, OR, USA). All other chemicals were purchased from Sigma-Aldrich (St. Louis, MO, USA)

Tissue Perfusion and Preparation

Organ preparation and perfusion for the rat vascularized composite allografts (hindlimbs), rat liver, rabbit kidney, and porcine ovary were performed at Tissue Testing Technologies LLC, UNC Charlotte, 21st Century Medicine, and Sylvatica Biotech Inc, respectively (Table 1). The specific details for each laboratory and tissue are given in the Supplemental Information. In short, the organs and VCAs were harvested and arteries were cannulated. The organ was then flushed with either Euro Collins buffer (Tissue Testing Technologies, UNC Charlotte, Sylvatica Biotech Inc) or Renasol-14 (21st Century Medicine) and cryoprotectants were introduced either continuously or through a series of steps until the tissue was deemed ready for vitirification. IONPs were delivered during the final loading step. Rat hindlimbs were also unloaded stepwise by flushing with a series of decreasing concentrations of cryoprotectant solution free of IONPs.

Rat hindlimbs, rat livers, and rabbit kidney were shipped to UMN at −80°C and warmed to 4°C for 48 h before imaging. The rat hindlimbs were immediately prepared for histology after MRI. The porcine ovaries were shipped overnight, on ice and stored at 4°C until imaging. Imaging of the porcine ovaries occurred within 48 h of perfusion. Rat livers, rabbit kidneys, and porcine ovaries were placed within a 50 mL PET centrifuge tube and surrounded by the perfusate solution. Rat hindlimbs were too large to fit into 50 mL PET centrifuge tubes and were instead measured inside plastic bags without surrounding

perfusate solution. After MRI, the porcine ovaries were imaged using μCT with the surrounding solution removed and then immediately prepared for histology.

Magnetic Resonance Image Acquisition

MR imaging was performed in a single session. All MR images were acquired with a volume transmit/receive coil having an inner diameter of 3 cm (Varian, Palo Alto, CA) in a 9.4-T 31-cm bore magnet (Magnex Scientific, Yarnton, UK) interfaced to a research console (Varian, Palo Alto, CA). Hindlimb VCAs were wrapped in a plastic bag before insertion into the volume coil. All organs were inserted into a 50 mL PET falcon tube and surrounded by the same solution that the organ contained (Euro Collins buffer, VS55, or M22) but without IONPs.

GRE acquisitions were used to produce two-dimensional (2D) R_2^* ($=1/T_2^*$) maps. Each image was acquired with bandwidth (BW) = 50 kHz, acquisition time = 2.56 ms, slice thickness = 5 mm, and resolution = 417 × 417 μm^2. GRE images were acquired with TR = 16 ms and TE = 9 ms. All 2D images were reconstructed using VnmrJ version 3.2.

The SWIFT 3D R_1 map was acquired using a Look-Locker method with a multi-band (MB) SWIFT sequence for image readout using flip angle = 1°, acquisition delay ≈ 2 μs, BW = 384 kHz, TR = 1.2 ms, gaps = 2, voxel resolution = 194 × 194 × 1172 μm^3, and total acquisition time around 7 min (17,22). The field-of view (FOV) was 50 × 50 × 150 mm^3 with image matrix size = 128 × 128 × 128 × 64 (x,y,z,t), N_{spiral} = 32, N_v = 4096, and 64 time points spaced linearly from 39.8 to 4596 ms were acquired. Within the rat liver R_1 maps, the 64 time points were amended to be spaced linearly from 12.7 to 1152 ms by adjusting N_v = 1024. MB-SWIFT images were reconstructed using an in-house program written in MATLAB (2012b) (22).

Relaxation maps were calculated using MATLAB (2012b). For each voxel, the time points were fit along the T_1 recovery curve using a three-variable exponential fit (17). The robustness of the exponential fit was tested for each voxel by adjusting the boundary values (23). Relaxation measurements were determined by least-squares fitting.

Microcomputer Tomography (μCT)

The surrounding solution was drained from the PET tube and samples were scanned in a μCT imaging system (Nikon XT H 225, Melville, NY) at voltage = 65 kV, current = 34 μA, and voxel resolution = 62 × 62 × 62 μm^3. Reconstruction was performed using 3D CT pro (Nikon Metrology) imported as unsigned 16-bit float images. Reconstruction was corrected for beam hardening, and background noise was minimized using a Hanning filter. Images were converted to Hounsfield units using an in-house program written in MATLAB (2012b).

Hybrid images with T_1-weighted MR images and R_1 mapping were aligned and scaled to match the μCT based on the location of the Teflon holders. The Teflon holders were masked out of the final images.

Histology

After imaging, the organs were fixed in 10% buffered formalin for a time period determined by the size of the sample. A one-month fixation was performed with the hindlimb, whereas the ovaries were fixed for 48 h. After fixation, the samples were rinsed well and placed into EDTA for decalcification. When the decalcification was complete, samples were blocked for routine processing and paraffin embedding. Tissue sections were cut at 4 μm and stained with Prussian blue and a nuclear fast red counterstain. Ovaries were also stained with anti-CD31 (Abcam, Cambridge, UK).

Results

The effects of IONPs (EMG-308, 179 mM_{Fe}; 10 mg_{Fe}/mL) perfused throughout the rat hindlimb are shown in Figure 1. Rat hindlimb is a very complex tissue, due to the presence of adipose, connective, bone, and muscular tissue. Some distinction between tissue structures, such as the bone (blue triangle) and muscle (yellow triangle), can be observed within the negative control (Figure 1.b). Within both the IONP loaded (Figure 1.c) and IONP washout (Figure 1.d) VCAs, negative contrast and pile-up artifacts are present at the location of the bone (blue triangle). Additionally, negative contrast is observed throughout the vasculature of the muscle (yellow triangle). Compared to the IONP-loaded tissue, the IONP washout tissue appears to have brighter contrast within the bone and less contrast within the muscle vasculature. The change in IONP distribution was not picked-up by the corresponding Prussian Blue histology, where the washout tissue appears similar to the negative control (see Supporting Information Figure S1). In the 3D image of the VCA following IONP unloading, no slice appeared to be completely free of IONPs when using voxel intensity as the metric.

The influence of solution composition for the IONP organ perfusion is observed in Figure 2. Similar to the rat hindlimb, the rat liver perfused with VS55 with EC containing IONPs (EMG-308, 357 mM_{Fe}; 20 mg_{Fe}/mL) produces a visually observed heterogenous distribution. This appeared as black spots surrounded by pink tissue throughout the organ (Figure 2.a). Within the corresponding MR image, pile-up artifacts obscure the image and the exact location of the organ cannot be discerned (Figure 2.b). A dramatic change in perfusion is observed when EC (plus EMG-308, 643 mM_{Fe}; 36 mg_{Fe}/mL) is used without CPAs. Visually, the organ appears to be an even brown color (Figure 2.c). An improvement was also observed within the T_1-weighted image, where lobes of the liver can be distinguished (Figure 2.d). Furthermore, only the EC perfused liver produced an R_1 map where the liver lobes could be distinguished from the surrounding solution (Supporting Information Figure S2).

Successful distribution within a leporine kidney perfused with a lower concentration (71 mM_{Fe}; 4 mg_{Fe}/mL) of IONPs (EMG-308) in M22 is shown in Figure 3.a. A GRE T_2*-weighted image produces negative contrast within the organ and large distortion artifacts (Figure 3.b), whereas MB-SWIFT T_1-weighted images provide contrast throughout the organ (Figure 3.c). Homogeneous distribution is not observed, however, the lack of homogeneity in signal is attributed to the different structures within the kidney, rather than aggregation or accumulation within capillaries. More specifically, a distinction in contrast

can be observed between the hilus, inner medulla, outer medulla, and cortex of the kidney. Similarly, the R_1 map indicates variation of IONP concentration throughout the kidney (Figures 3.d and 3.e). The highest IONP concentration is located at the renal artery (blue triangle) and a reliable relaxation fitting could not be calculated, which is expected based on previously determined robustness criteria (23).

The effect of IONP coating is shown with porcine ovaries in Figure 4 with the perfusion of a high concentration of PEG-coated IONP to maintain stability (PBG-300, 429 mM_{Fe}; 24 mg_{Fe}/mL) in VS55. The ovary perfusions were considered a success in that, visually, the organ was evenly brown. The T_1-weighted negative control image (Figure 4.a) demonstrates barely any distinction between the surrounding solution and tissue. However, image contrast is visible within the IONP loaded tissue, including distinct features in follicles of the ovaries (Figure 4.b). The R_1 map shows an increase in R_1 compared to the negative control (Figures 4.c & d), however, some of the detail is lost. An increase in R_1 is observed within the surrounding solution ($R_1 < 1\ s^{-1}$) and the ovary ($R_1 = 1.1 – 1.4\ s^{-1}$), when comparing the IONP-loaded ovary with the negative control (Figure 4.e). Histology with both Prussian Blue staining and anti-CD31 (vasculature) staining (brown) shows that the IONPs are only present within the vasculature of the ovary (Figures 5). The loss of IONPs during the fixation process was visually evident (Supporting Information Figure S3). Finally, T_1-weighted images, R_1 maps, and μCT images were compared over the range of IONP concentrations within the ovary (Figure 6). The T_1-weighted images demonstrate pile-up artifacts obscuring the location of the ovarian artery. Additionally, the vasculature visible with μCT indicates the high IONP concentration, which is better observed with the R_1 map. A histogram analysis across the entirety of the R_1 map demonstrates the similar two peak pattern shown in Figure 3.e. A similar analysis across the entirety of the μCT image indicates a gaussian distribution of values around 400 HU; however, an ROI drawn over an artery demonstrates the elevation to ~ 800 HU, which is distinctly different from the background of the surrounding tissue. A video of a 3D brightest point projection for the R_1 map and μCT is also included in the supplemental information (Supporting Information Video S1).

Discussion

The work described herein provides early examples of how MR imaging can play a critical role in assessing organs and VCAs perfused ex vivo with IONPs, in preparation for cryopreservation and nanowarming. Imaging of tissue perfusion with MRI typically refers to *in vivo* organ blood-flow with or without contrast agents, as extensively utilized in the clinic (24–26). Conversely, *ex vivo* perfusion MRI focuses on tissues perfused and fixed with formalin (27). Contrast agents have been applied to *ex vivo* perfusion MRI (28,29). Cryopreservation and nanowarming requires perfusion of the organ with CPAs that prevent crystallization of the tissue at cryogenic temperatures (7,8). Successful nanowarming requires the use of high IONP concentrations (≥ 179 $mM_{Fe;}$ 10 mg_{Fe}/mL), which are added to the CPA in the last step of perfusion (10,30). Therefore, contrast within these organs is due mainly to the presence of IONPs. The impact of IONPs on contrast for specific organs has been discussed at length, after i.t. and i.v. injection of IONPs *in vivo* (31); However, perfused *ex vivo* organ systems behave differently from *in vivo* organs which could impact

signal relaxation. Therefore, organs and VCAs perfused for cryopreservation and nanowarming present an interesting new system, different from other MRI perfusion models or IONP applications.

The selection of perfusate or CPA can have a profound impact on imaging. Many of the formulations, such as VS55 and M22, incorporate a number of organic compounds in addition to water (32–34). Therefore, pulse sequences with a smaller bandwidth (e.g., 50 kHz used in the GRE sequence) will be prone to have image blurring and chemical shift artifacts, which the large bandwidth of MB-SWIFT (384 kHz) substantially reduces. In addition to image artifacts, a change in perfusate composition can have a dramatic impact on IONP distribution. We observe that EC carrier solution alone produces an even distribution of IONPs throughout the liver compared to the much more viscous VS55 formulation in EC (11,15). Previous work has demonstrated the importance of IONP stability (ability to remain in solution) for imaging applications in vitro, in vivo and in CPA perfused systems (10,35). Additionally, nanowarming is dependent on IONPs maintaining good heating properties, which can also be compromised with unstable IONPs (11,35). Within this work, we observed the importance of IONP stability for homogeneous distribution of IONPs through the organ and imaging. For instance, in the hindlimb and liver the use of uncoated EMG-308 within VS55 led to aggregation and imaging artifacts. Whereas, within the ovary and kidney PEGylated PMG-300 in VS55 and EMG-308 in M22, respectively, were sufficiently stable to allow a more homogenous distribution without aggregation and imaging artifacts. Therefore, future development of IONPs for cryopreservation applications needs to focus on stability within specific CPAs.

The R_1 maps within the hypothermic perfused organs demonstrate the potential to localize and quantify IONPs. Therefore, it is feasible that these measurements could allow for the estimation of locally achievable heating rates based on the known specific absorption rates (SAR_{Fe}) of particular IONPs (16). The quantitative range of Ferrotec EMG-308 was previously evaluated to be reliable up to 35.71 mM_{Fe} (2 mg_{Fe}/mL) in 1% agarose, but changes in R_1 background were not evaluated (16), and the R_1 background change caused by both tissue and the CPA could reduce the range of quantifiable IONP concentrations. Previous research on *in vivo* systems demonstrated the organ dependence on the correlation between R_1 and IONP concentration, as well as the SAR_{Fe} (16). However, it is incorrect to assume that the behavior of IONPs within the perfused tissue will be the same as *in vivo*. IONPs *in vivo* circulate throughout the whole body at physiological temperatures and have uptake into the reticuloendothelial system organs (i.e. predominately liver and spleen) (16). The hypothermic perfused tissue system exhibits a drastically different response, due to the isolation of a single tissue and slowed metabolic functions. Both the hindlimb and ovaries show no indications of macrophage uptake. It is therefore conceivable within perfused organs and VCAs the difference in background relaxation rates could have the largest impact on the range of IONP concentration quantification. The range of relevant R_1 values was observed to be distinct for each organ (liver 0 – 6 s^{-1}; kidney 0 – 3.5 s^{-1}, ovary 1 – 2 s^{-1}), but the reason(s) for this difference between organ systems is not yet understood. Clearly, further investigation is necessary to establish the limitations, capabilities, and background effects of R_1 mapping with organs and VCAs prepared for nanowarming.

Prussian blue histology is considered the gold standard for the localization of iron within tissues (16,31,36–38). In the present studies, we found Prussian blue staining to be an unreliable method for IONP localization within the vasculature. For example, the concentration of IONPs (or blue staining) within the vasculature was not consistent throughout the IONP-loaded ovaries (Supporting Information Figure S3). This could indicate that the IONPs were not well dispersed; however, that conclusion would be inconsistent with observations from μCT and MRI. Histology from the hindlimbs demonstrated similar issues. Iron staining is visible within the IONP-loaded hindlimb where high concentrations (179 mM_{Fe},10 mg_{Fe}/mL) of IONPs were still present (Supporting Information Figure S1). Our observation of IONP loss during the 48 h fixation step (Supporting Information Figure S4) is consistent with previous reports about the difficulty to properly stain unbound iron using Prussian Blue staining (39). Therefore, Prussian blue staining was determined to be an inadequate assessment method for IONP distribution within organs and VCAs prepared for cryopreservation.

A previous evaluation measured the upper limit of EMG-308 quantification with SWIFT to be 35.7 mM_{Fe} (2 mg_{Fe}/mL) (23). Therefore, the resolved image obtained from liver following perfusion with EC containing IONPs at a concentration of 642.9 mM_{Fe} (36 mg_{Fe}/mL) was unanticipated. μCT is an ideal quantitative IONP measurement for concentrations above 179 mM_{Fe} (40,41). Composite images of the ovary demonstrate that pile-up artifacts observed in the T_1-weighted images correlate to locations of high IONP concentration. Additionally, the R_1 map shows variation within regions where the μCT signal cannot be differentiated from the background of the tissue. Future studies will compare the merits and overlap for non-invasively quantifying IONPs with both μCT and MRI.

The tissue images shown here document some of the first attempts at achieving cryopreservation through perfusion with CPAs impregnated with IONPs for nanowarming. More work is necessary to fully understand the utility of MRI within this system. Future imaging work will focus on testing quantitative R_1 mapping on simpler and high demand organ systems, such as the liver, kidney, heart, and ovaries. The ability to acquire quantitative images will accelerate the development of cryopreservation with nanowarming as protocols are optimized to more homogeneously perfuse IONPs through organs. Future nanowarming research will increasingly concentrate on transitioning from proof-of-principle physical studies such as those described here toward demonstrating organ viability.

Conclusion

The perfusion of organs and VCAs with IONP solutions for nanowarming is a technology still under development with a need for better assessment methods. Herein, we demonstrate the first attempts at imaging several types of *ex vivo* organs and VCAs perfused with IONPs for cryopreservation and nanowarming. Histology is typically considered to be the gold standard for iron distribution, but was determined to be an inadequate method for subnormothermic perfused organs and VCAs. T_1-weighted MRI provides a non-invasive method for rapid assessment of IONP distribution, and as such, might be used to accelerate the optimization of nanowarming. Initial studies demonstrate the use of MRI assessment of

organs perfused with IONP concentrations at 642.9 mM_{Fe} (36 mg_{Fe}/mL). More studies are necessary to fully characterize the utility of the quantitative images acquired to provide accurate IONP concentrations.

Supplementary Material

Refer to Web version on PubMed Central for supplementary material.

Acknowledgements

This work was funded by: NIH P41 EB015894, R01 HL135046 and R01 DK117425, WM KECK Foundation, and U.S. Army Medical Research and Development Command contract no. W81XWH-16-1-0508 and no. W81XWH-16-C-0057. The views, opinions, and findings contained in this report are those of the authors and should not be construed as an official Department of the Army position, policy, or decision unless so designated by other documentation. Research on rabbit kidneys was supported in part from institutional funding from 21st Century Medicine, Inc. Histologic services were provided by the Histology and Immunohistochemistry (IHC) Laboratory, University of Minnesota. Histologic imaging was provided by the University of Minnesota Imaging Center. The authors thank C. Forster for her support with histology. We acknowledge N. Manuchehrabadi for his input during the onset of this project. We acknowledge John Phan and Victor Vargas for their assistance with rabbit kidney perfusion, and Simona Baicu for contribution to ovary cannulation and perfusion procedures.

References

1. Giwa S, Lewis JK, Alvarez L, Langer R, Roth AE, Church GM, Markmann JF, Sachs DH, Chandraker A, Wertheim JA, Rothblatt M, Boyden ES, Eidbo E, Lee WPA, Pomahac B, Brandacher G, Weinstock DM, Elliott G, Nelson D, Acker JP, Uygun K, Schmalz B, Weegman BP, Tocchio A, Fahy GM, Storey KB, Rubinsky B, Bischof J, Elliott JAW, Woodruff TK, Morris GJ, Demirci U, Brockbank KGM, Woods EJ, Ben RN, Baust JG, Gao D, Fuller B, Rabin Y, Kravitz DC, Taylor MJ, Toner M. The promise of organ and tissue preservation to transform medicine. Nature Biotechnology 2017;35:530.
2. Lewis JK, Bischof JC, Braslavsky I, Brockbank KG, Fahy GM, Fuller BJ, Rabin Y, Tocchio A, Woods EJ, Wowk BG, Acker JP, Giwa S. The Grand Challenges of Organ Banking: Proceedings from the first global summit on complex tissue cryopreservation. Cryobiology 2015.
3. Fahy GM, MacFarlane DR, Angell CA, Meryman HT. Vitrification as an approach to cryopreservation. Cryobiology 1984;21(4):407–426. [PubMed: 6467964]
4. Mazur P. Freezing of Living Cells: Mechanisms and Implications. American Journal of Physiology-Cell Physiology 1984;247(3):C125–C142.
5. Han B, Bischof JC. Engineering Challenges in Tissue Preservation. Cell Preservation Technology 2004;2(2):91–112.
6. Karlsson JO, Toner M. Long-term storage of tissues by cryopreservation: critical issues. Biomaterials 1996;17(3):243–256. [PubMed: 8745321]
7. Song YC, Khirabadi BS, Lightfoot F, Brockbank KG, Taylor MJ. Vitreous cryopreservation maintains the function of vascular grafts. Nat Biotechnol 2000;18(3):296–299. [PubMed: 10700144]
8. Taylor MJ, Song YC, Brockbank KGM. Vitrification in Tissue Preservation: New Developments Life in the Frozen State: CRC Press; 2004.
9. Fahy GM, Wowk B. Principles of cryopreservation by vitrification. Methods Mol Biol 2015;1257:21–82. [PubMed: 25428002]
10. Manuchehrabadi N, Gao Z, Zhang J, Ring HL, Shao Q, Liu F, McDermott M, Fok A, Rabin Y, Brockbank KGM, Garwood M, Haynes CL, Bischof JC. Improved tissue cryopreservation using inductive heating of magnetic nanoparticles. Science Translational Medicine 2017;9(379).
11. Etheridge ML, Hurley KR, Zhang J, Jeon S, Ring HL, Hogan C, Haynes CL, Garwood M, Bischof JC. Accounting for biological aggregation in heating and imaging of magnetic nanoparticles. Technology 2014;02(03):214–228.

12. Partington MT, Acar C, Buckberg GD, Julia PL. Studies of retrograde cardioplegia. II. Advantages of antegrade/retrograde cardioplegia to optimize distribution in jeopardized mycardium. J Thorac Cardiovasc Surg 1989;97(4):613–622. [PubMed: 2927165]
13. Fahy GM, Wowk B, Wu J, Phan J, Rasch C, Chang A, Zendejas E. Cryopreservation of organs by vitrification: perspectives and recent advances. Cryobiology 2004;48(2):157–178. [PubMed: 15094092]
14. Fahy GM, Wowk B, Pagotan R, Chang A, Phan J, Thomson B, Phan L. Physical and biological aspects of renal vitrification. Organogenesis 2009;5(3):167–175. [PubMed: 20046680]
15. Hurley KR, Ring HL, Etheridge M, Zhang J, Gao Z, Shao Q, Klein ND, Szlag VM, Chung C, Reineke TM, Garwood M, Bischof JC, Haynes CL. Predictable Heating and Positive MRI Contrast from a Mesoporous Silica-Coated Iron Oxide Nanoparticle. Molecular Pharmaceutics 2016.
16. Zhang J, Ring HL, Hurley KR, Shao Q, Carlson CS, Idiyatullin D, Manuchehrabadi N, Hoopes PJ, Haynes CL, Bischof JC, Garwood M. Quantification and biodistribution of iron oxide nanoparticles in the primary clearance organs of mice using T1 contrast for heating. Magnetic Resonance in Medicine 2017;78(2):702–712. [PubMed: 27667655]
17. Zhang J, Chamberlain R, Etheridge M, Idiyatullin D, Corum C, Bischof J, Garwood M. Quantifying iron-oxide nanoparticles at high concentration based on longitudinal relaxation using a three-dimensional SWIFT look-locker sequence. Magnetic Resonance in Medicine 2014;71(6): 1982–1988. [PubMed: 24664527]
18. Corot C, Robert P, Idée J-M, Port M. Recent advances in iron oxide nanocrystal technology for medical imaging. Advanced Drug Delivery Reviews 2006;58(14):1471–1504. [PubMed: 17116343]
19. Ring HL, Zhang J, Klein ND, Eberly LE, Haynes CL, Garwood M. Establishing the overlap of IONP quantification with echo and echoless MR relaxation mapping. Magnetic Resonance in Medicine 2017(early view).
20. Brockbank KGM, Chen Z, Greene ED, Campbell LH. Vitrification of Heart Valve Tissues In: Wolkers WF, Oldenhof H, editors. Cryopreservation and Freeze-Drying Protocols. New York, NY: Springer New York; 2015 p 399–421.
21. Fahy GM, Wowk B, Wu J, Phan J, Rasch C, Chang A, et al. Cryopreservation of Organs by Vitrification: Perspectives and Recent Advances. Cryobiology 2004;48(2):157–178. [PubMed: 15094092]
22. Idiyatullin D, Corum CA, Garwood M. Multi-Band-SWIFT. Journal of Magnetic Resonance 2015;251(0):19–25. [PubMed: 25557859]
23. Ring HL, Zhang J, Klein ND, Eberly LE, Haynes CL, Garwood M. Establishing the overlap of IONP quantification with echo and echoless MR relaxation mapping. Magnetic Resonance in Medicine 2017;79(3):1420–1428. [PubMed: 28653344]
24. Pandharipande PV, Krinsky GA, Rusinek H, Lee VS. Perfusion Imaging of the Liver: Current Challenges and Future Goals. Radiology 2005;234(3):661–673. [PubMed: 15734925]
25. Kim MN, Durduran T, Frangos S, Edlow BL, Buckley EM, Moss HE, Zhou C, Yu G, Choe R, Maloney-Wilensky E, Wolf RL, Grady MS, Greenberg JH, Levine JM, Yodh AG, Detre JA, Kofke WA. Noninvasive measurement of cerebral blood flow and blood oxygenation using near-infrared and diffuse correlation spectroscopies in critically brain-injured adults. Neurocritical care 2010;12(2):173–180. [PubMed: 19908166]
26. Jin T, Kim S. Spatial dependence of CBV-fMRI: a comparison between VASO and contrast agent based methods. 2006 30 8−3 Sept. 2006 p 25–28.
27. Roebroeck A, Miller KL, Aggarwal M. Ex vivo diffusion MRI of the human brain: Technical challenges and recent advances. NMR in Biomedicine 2018;0(0):e3941.
28. Holmes HE, Powell NM, Ma D, Ismail O, Harrison IF, Wells JA, Colgan N, O'Callaghan JM, Johnson RA, Murray TK, Ahmed Z, Heggenes M, Fisher A, Cardoso MJ, Modat M, O'Neill MJ, Collins EC, Fisher EMC, Ourselin S, Lythgoe MF. Comparison of In Vivo and Ex Vivo MRI for the Detection of Structural Abnormalities in a Mouse Model of Tauopathy. Frontiers in Neuroinformatics 2017;11:20. [PubMed: 28408879]

29. Poduslo JF, Wengenack TM, Curran GL, Wisniewski T, Sigurdsson EM, Macura SI, Borowski BJ, Jack CR. Molecular Targeting of Alzheimer's Amyloid Plaques for Contrast-Enhanced Magnetic Resonance Imaging. Neurobiology of Disease 2002;11(2):315–329. [PubMed: 12505424]
30. Etheridge ML, Xu Y, Rott L, Choi J, Glasmacher B, Bischof JC. Radiofrequency Heating of Magnetic Nanoparticles Improves the Thawing of Cryopreserved Biomaterials. Technology (open access online) 2014.
31. Ring HL, Bischof JC, Garwood M. The Use and Safety of Iron-Oxide Nanoparticles in MRI and MFH In: Shrivastava D, editor. Handbook - RF Safety: eMagRes; 2019.
32. Guan N, Blomsma SA, van Midwoud PM, Fahy GM, Groothuis GMM, de Graaf IAM. Effects of cryoprotectant addition and washout methods on the viability of precision-cut liver slices. Cryobiology 2012;65(3):179–187. [PubMed: 22722061]
33. Mukherjee IN, Li Y, Song YC, Long RC Jr., Sambanis A. Cryoprotectant transport through articular cartilage for long-term storage: experimental and modeling studies. Osteoarthritis and Cartilage 2008;16(11):1379–1386. [PubMed: 18539055]
34. Brockbank KGM, Wright GJ, Yao H, Greene ED, Chen ZZ, Schenke-Layland K. Allogeneic Heart Valve Storage Above the Glass Transition at −80°C. The Annals of Thoracic Surgery 2011;91(6): 1829–1835. [PubMed: 21536250]
35. Hurley KR, Ring HL, Etheridge M, Zhang J, Gao Z, Shao Q, Klein N, Szlag VM, Chung C, Reineke TM, Garwood M, Bischof J, Haynes CL. Predictable Heating and Positive MRI Contrast from a Mesoporous Silica-Coated Iron Oxide Nanoparticle. Mol Pharm 2016;13(7):2172–2183. [PubMed: 26991550]
36. Tate JA, Kett W, Ndong C, Griswold KE, Hoopes PJ. Biodistribution of antibody-targeted and non-targeted iron oxide nanoparticles in a breast cancer mouse model. Proceedings of SPIE--the International Society for Optical Engineering 2013;8584:85840G.
37. Tate JA, Petryk AA, Giustini AJ, Hoopes PJ. In vivo biodistribution of iron oxide nanoparticles: an overview. Proceedings of SPIE 2011;7901:790117. [PubMed: 24478825]
38. Hoopes PJ, Strawbridge RR, Gibson UJ, Zeng Q, Pierce ZE, Savellano M, Tate JA, Ogden JA, Baker I, Ivkov R. Intratumoral Iron Oxide Nanoparticle Hyperthermia and Radiation Cancer Treatment. Thermal Treatment of Tissue: Energy Delivery and Assessment; 2007 (Thermal Treatment of Tissue: Energy Delivery and Assessment).
39. Sands SA, Leung-Toung R, Wang Y, Connelly J, LeVine SM. Enhanced Histochemical Detection of Iron in Paraffin Sections of Mouse Central Nervous System Tissue: Application in the APP/PS1 Mouse Model of Alzheimer's Disease. ASN neuro 2016;8(5):1759091416670978.
40. Etheridge ML, Xu Y, Rott L, Choi J, Glasmacher B, Bischof JC. RF heating of magnetic nanoparticles improves the thawing of cryopreserved biomaterials. TECHNOLOGY (open access: http://wwwtechnologythejournalcom) 2014;2(3):1–14.
41. Gneveckow U, Jordan A, Scholz R, Brüss V, Waldöfner N, Ricke J, Feussner A, Hildebrandt B, Rau B, Wust P. Description and characterization of the novel hyperthermia-and thermoablation-system MFH300F for clinical magnetic fluid hyperthermia. Medical physics 2004;31:1444–1444. [PubMed: 15259647]

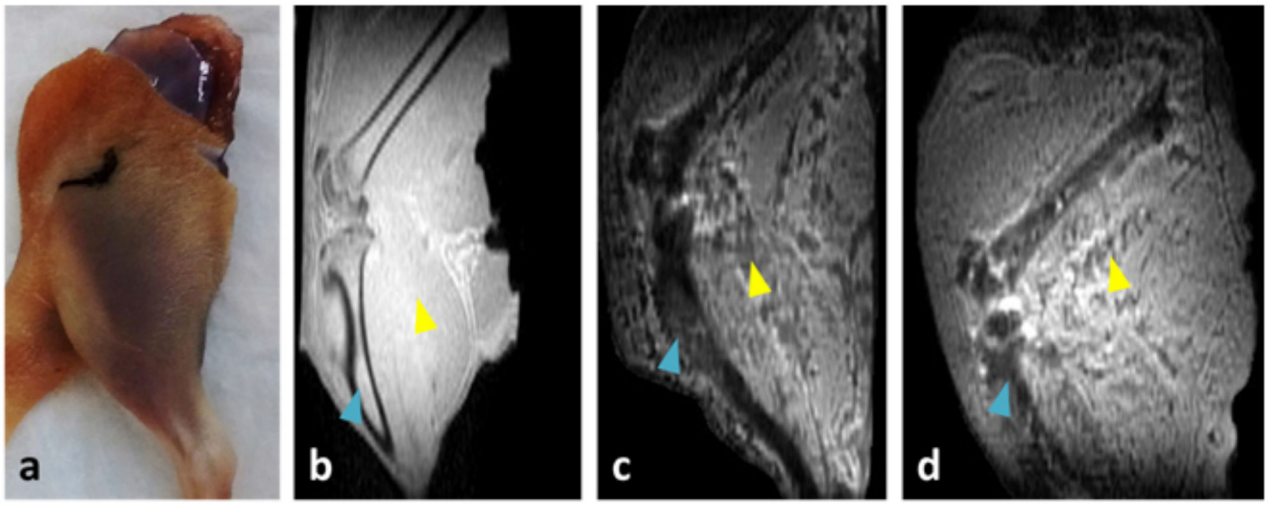

Figure 1:

Imaging of rat hindlimb. Photo of rat hindlimb post-perfusion (a). MB-SWIFT T_1-weighted images of hindlimbs perfused with VS55 (b), VS55 with IONPs (EMG-308, 179 mMFe; 10 mgFe/mL) (c), and unloaded after perfusion with VS55 with IONPs (d). The blue triangles mark the location of the tibia. The yellow triangles mark the location of the muscle. In the case of (c) and (d), pile-up artifacts are visible within the muscle.

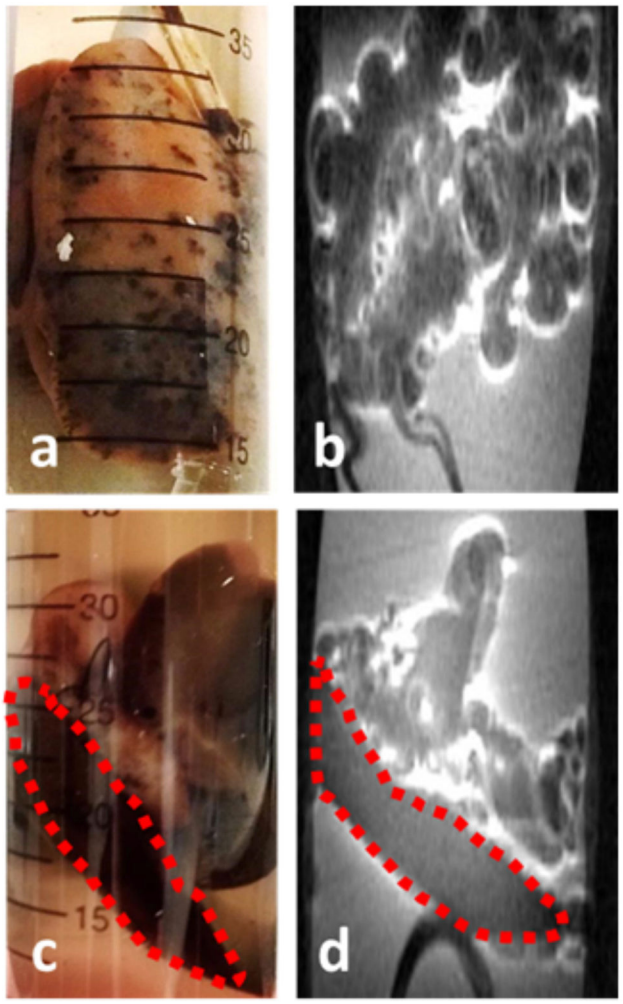

Figure 2:
The difference in distribution from rat livers perfused with IONPs (EMG-308) using VS55 and EC as the perfusate. The rat liver perfused with VS55 and 357 mM_{Fe} (20 mg_{Fe}/mL) demonstrated a very heterogeneous distribution (a) which resulted in pile-up artifacts obscuring the image (b). The rat liver perfused with EC and 643 mM_{Fe} (36 mg_{Fe}/mL) demonstrated a more homogeneous distribution (c), which resulted in a relatively artifact free image (d).

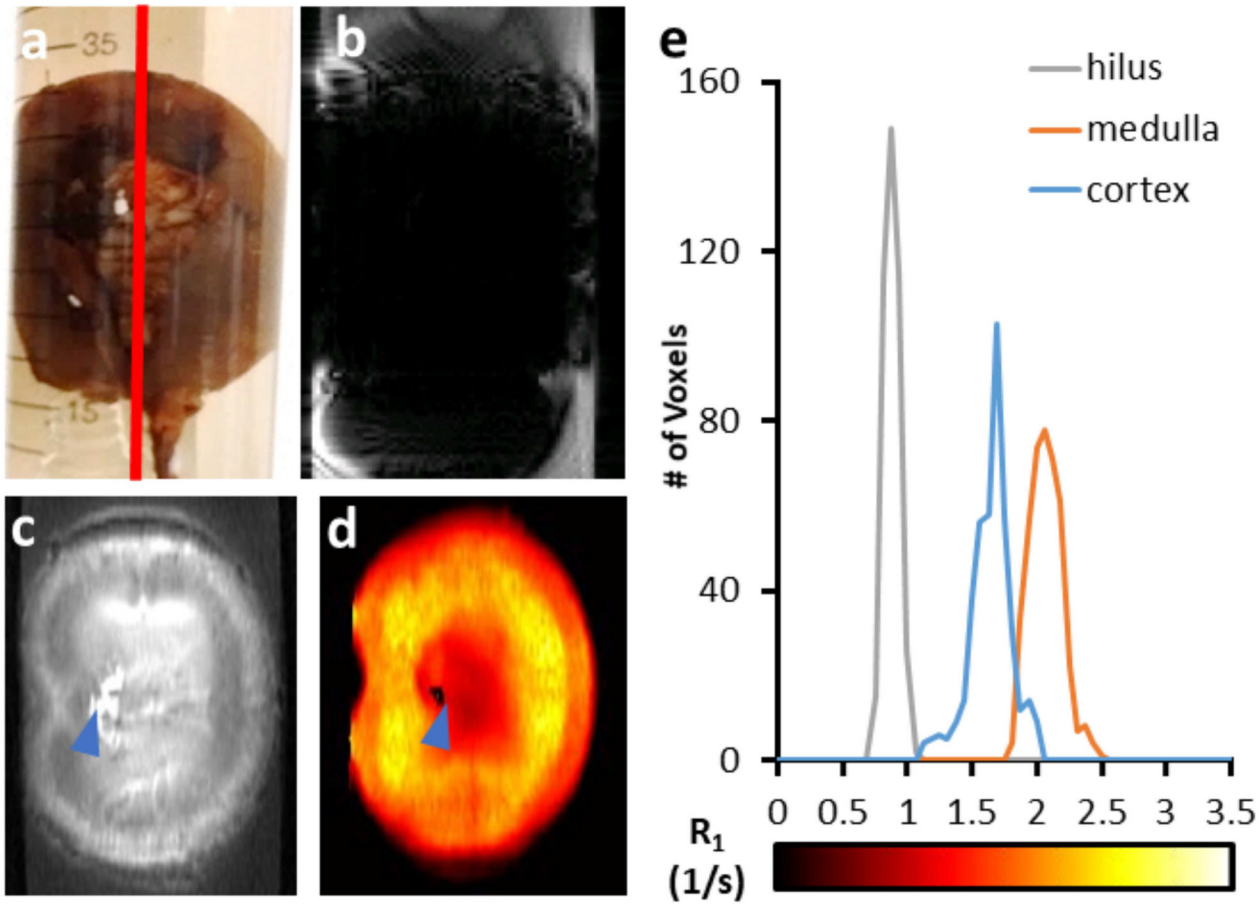

Figure 3:

The distribution of IONPs (EMG-308; 71 mM_{Fe}) is visually homogeneous in the rabbit kidney when perfused with M22 (a). A GRE image of the rabbit kidney demonstrates negative contrast and very large artifacts (b). The T_1-weighted MB-SWIFT image demonstrates contrast throughout the kidney (c). The R_1 map further indicates variation in IONP concentration throughout the structure of the kidney (d). A 2.9 × 5.8 mm^2 (15 × 30 voxel) ROI was drawn within the hilus, medulla, and cortex to demonstrate the difference in R_1 between these anatomical regions (e).

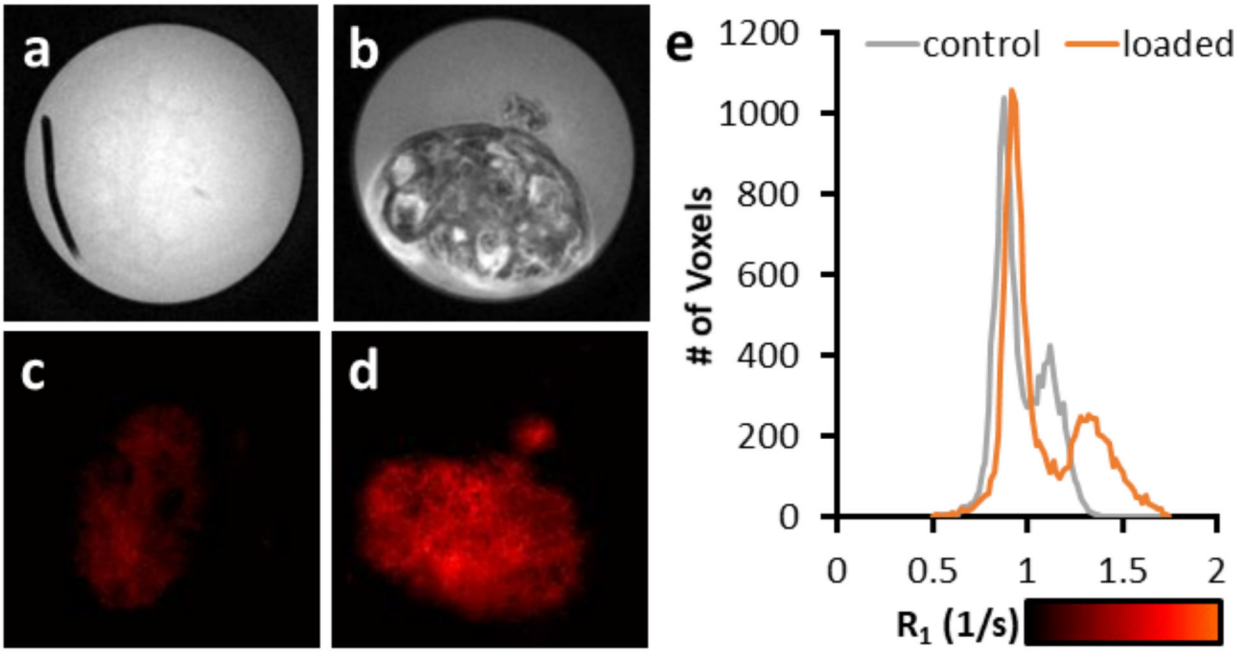

Figure 4:

A comparison of T_1-weighted images from porcine ovaries perfused with VS55 (a) and IONPs (PMG-300; 429 mM_{Fe}) (b). The IONP perfused ovary allows for the visualization of the follicles of the ovary. Changes in R_1 can be observed from the porcine ovaries perfused with VS55 (c) and IONPs (d). The R_1 increases by 0.21 s^{-1} between the VS55 and IONP perfused ovary (e).

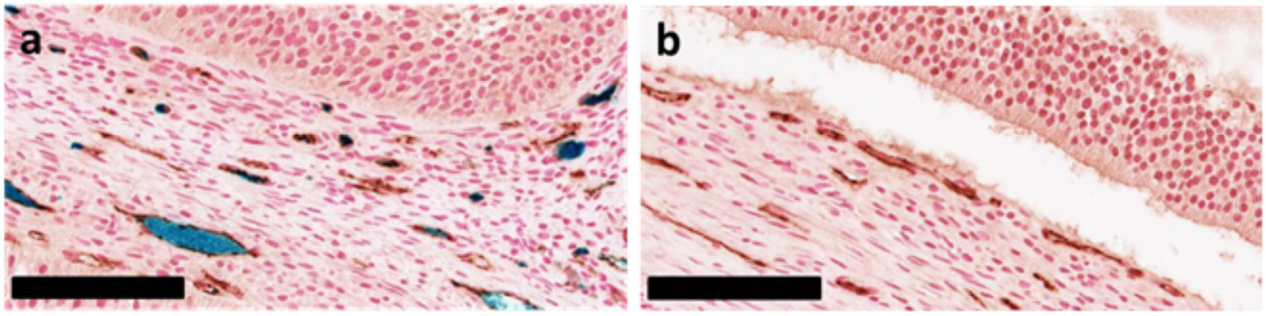

Figure 5:

A comparison of Prussian blue stained histology for IONP (PBG-300, 429 mM_{Fe}) in VS55 (left) and VS55 perfused ovary (right). The IONP perfused ovary demonstrates some loss of IONPs during the fixation process (lower right corner). Black scale bar indicates 100 μm.

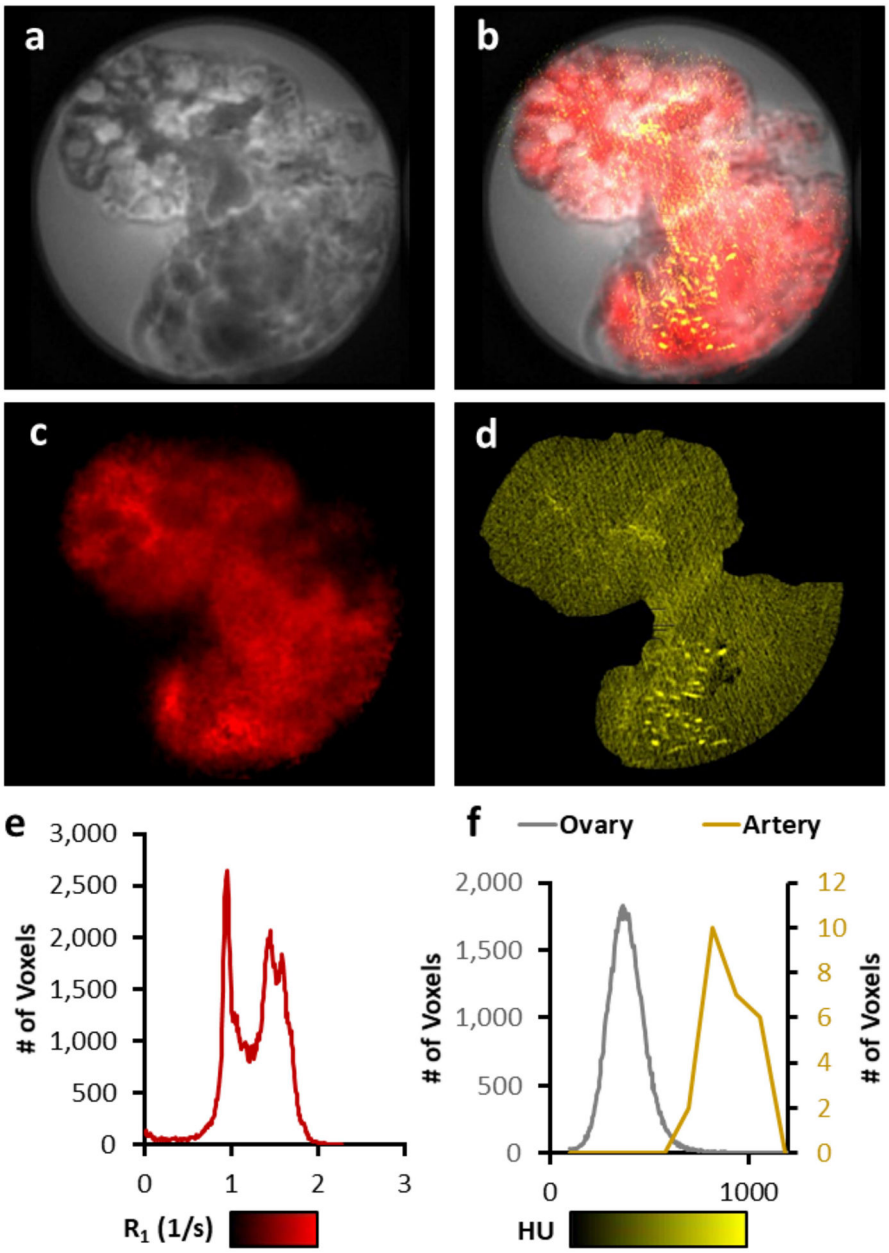

Figure 6:

A comparison of MRI and μCT imaging capability. The T_1-weighted image of ovary perfused with IONPs (a) shows a region where IONP concentration is visible within the ovary using MB-SWIFT T_1-weighted imaging (white circle) and a region where pile-up artifacts are visible due to the high concentration within the ovarian artery (blue circle) (a). An overlap of the T_1-weighted images of ovary with R_1 mapping (red) and μCT (yellow) demonstrate that the high concentration of IONP causing pile-up artifacts are visible using μCT (blue circle), and that μCT is unable to be resolved from the VS55 background within the ovary (white circle) (b). The R_1 map (1 to 2 s^{-1}) demonstrates some variation in R_1

across the tissue (c & e). The μCT in Hounsfield units (100 to 1000 HU) shows a similar background across the tissue, but high HU within the vasculature (blue arrow/artery) (d & f).

Table 1:

Tissue Preparation

Animal Model	Tissue	Perfusion Location	Solution	IONP Type	Perfusate IONP Concentration	
					(mM_{Fe})	(mg_{Fe}/mL)
murine	hindlimb	Tissue Testing Technologies	VS55	EMG-308	179	10
murine	liver	UNC Charlotte	EC VS55	EMG-308 EMG-308	643 357	36 20
leporine	kidney	21st Century Medicine	M22	EMG-308	71	4
porcine	ovary	Sylvatica Biotech Inc	VS55	PMG-300	429	24